# Designing High Corrosion Resistant Peritectic Magnesium Alloys *via* Sc and Y Addition

PENGYU ZHAO, TIAN XIE, XINMEI XU, HONG ZHU, FUYONG CAO, TAO YING, and XIAOQIN ZENG

With the help of density functional theory (DFT) calculations, Mg-Sc-Y alloys with various Y content were designed and produced. The single-phase Mg-Sc-Y alloys were composed of a typical peritectic microstructure with internal Sc-rich zones surrounded by Y-rich zones. With increasing Y content, the hydrogen evolution rates decreased significantly to 0.13 mL/cm$^2$/day and increased slightly afterward. This was attributed to the combined effect of a decrease in the thermodynamic driving force for corrosion, surface layer improvement, and an increase in the number of galvanic couples between the Sc-rich and Y-rich zones.

## I. INTRODUCTION

MAGNESIUM (Mg) alloys are considered one of the candidates for engineering applications in the automobile and aeronautical industry, owing to their good castability and high strength-to-weight ratio (specific strength).[1–4] However, the poor corrosion resistance of these alloys has significantly restricted their application.[5–10] Mg is quite susceptible to corrosion due mainly to its negative potential ($\sim -2.37$ V$_{SHE}$)[11] and low Pilling–Bedworth (P–B) ratio ($< 1$).[12,13] These factors are conducive for the occurrence of galvanic corrosion and hinder the formation of a protective passive film on the alloys surface.

Previous studies[12,14–16] have demonstrated improvements in the corrosion performance of Mg by controlling micro-galvanic corrosion, *i.e.*, by designing a single-phase Mg alloy. To mimic the designing concept of stainless steel, the development of "stainless" Mg alloy must satisfy three requirements, namely (i) the alloying elements should exhibit high solid solubility in Mg, thereby resulting in maximum enhancement of the solid solution strengthening and the passivation behavior of the elements. (ii) The alloying elements should form a protective corrosion layer. The P–B ratio of the added elements, which elucidates the coverage integrity of the passive films on the surface of the alloys, should be higher than 1. (iii) The differences in electrode potential between the alloying element (M)-rich zone and depleted zone should be small, so as to reduce the susceptibility of the alloy to corrosion.

Based on the aforementioned three requirements, a summary of the potential alloying elements is presented[17–20] in Figure 1. Among these elements, scandium (Sc) appears to be a potential choice for designing Mg alloys with high corrosion resistance. Additionally, compared with other rare earth elements, Sc yields greater grain size refinement[20,21] and comparable levels of anode-kinetics suppression.[12] Unlike most alloying elements such as Al and Zn, who tend to form the eutectic system (a liquid phase decomposes into a homogeneous solid mixture of two or more substances during cooling) with Mg, Sc leads to the preferential formation of a peritectic system (a liquid phase reacts with a solid phase during cooling to produce a second solid phase) with Mg, thereby resulting in Sc-rich zones and Sc-depleted areas and, consequently, micro-galvanic corrosion. To further improve the corrosion resistance of the Mg-Sc system, the element yttrium (Y), which forms a eutectic system with Mg, is added to the system. This addition is based on the premise that Y will alter the electrode potential of Sc-depleted zones,[22] thus lowering the driving force for micro-galvanic corrosion.

PENGYU ZHAO, TIAN XIE, and XINMEI XU are with the National Engineering Research Center of Light Alloy Net Forming, School of Materials Science and Engineering, Shanghai Jiao Tong University, Shanghai 200240, P.R. China. HONG ZHU is with the University of Michigan - Shanghai Jiao Tong University Joint Institute, Shanghai Jiao Tong University, Shanghai 200240, P.R. China and also with the State Key Lab of Metal Matrix Composites, Shanghai Jiao Tong University, Shanghai 200240, P.R. China. FUYONG CAO is with the Center for Marine Materials Corrosion and Protection, College of Materials, Xiamen University, Xiamen 361005, P.R. China. TAO YING is with the National Engineering Research Center of Light Alloy Net Forming, School of Materials Science and Engineering, Shanghai Jiao Tong University. Contact email: yingtao85@sjtu.edu.cn XIAOQIN ZENG is with the National Engineering Research Center of Light Alloy Net Forming, School of Materials Science and Engineering, Shanghai Jiao Tong University and also with the State Key Lab of Metal Matrix Composites, Shanghai Jiao Tong University. Contact email: xqzeng@sjtu.edu.cn

Therefore, this study is aimed at designing Mg alloys with high corrosion resistance. Computational simulations and experimental tests are conducted to investigate the corrosion performance and the underlying corrosion mechanism of the designed Mg-Sc-Y alloys.

## II. THEORY CALCULATIONS

Available data on the electrode potential differences in the Sc-rich zone and Sc-depleted zone are limited and therefore, DFT calculations are used to determine the driving force of corrosion in ternary Mg-Sc-Y alloys. The work function ($\phi$), defined as the minimum energy required to remove an electron from a metal, is closely correlated with the thermodynamic driving force of corrosion. This function can be calculated as the energy difference between the vacuum level and the Fermi level of the slab model and is given as follows[23,24]:

$$\phi = \Phi_{vac} - E_{fermi} \quad [1]$$

$\Phi_{vac}$ is the vacuum energy, and $E_{fermi}$ is the Fermi level of the slab.

Therefore, the work functions of pure Mg and Mg-Sc as well as Mg-Y solid solutions were calculated *via* DFT using the Vienna *Ab initio* Simulation Package (VASP),[25] the Perdew–Burke–Ernzerhof functional (PBE),[26] and the projector augmented wave (PAW)[27] method. As Figure 2(a) illustrates, a 5×5 Mg (0001) supercell containing eight Mg layers was built as the slab model (200 atoms in total). The model was separated by a 20 Å vacuum region, to prevent vertical interactions between the monolayers and its periodic images.[28] To simulate the Mg-Sc and Mg-Y solid solutions, the Mg atoms on the surface of the pure Mg slab model were, respectively, replaced, as shown in Figures 2(b) through (e). The plane wave with kinetic energy cutoff of 520 eV was settled, and Γ-centered k-meshes of $1 \times 1 \times 1$ were used for the structural optimization and static calculations. During the structural optimization, all atoms were relaxed, whereas they were all fixed during the static calculation process. The electronic convergence criterion was set to $1 \times 10^{-3}$ meV in the static calculation, to obtain accurate energy and electrostatic potential inside the materials.

To avoid Fermi level bending caused by the nanoeffect of the surface state, the Fermi level was corrected in accordance with Ramprasad,[29] rather than being read directly from the VASP. Firstly, the energy difference ($\Delta V$) between the Fermi level and the internal average electrostatic potential level in the pure Mg bulk material was calculated. Then, the average electrostatic potential of the complete block period ($E_{average}$) was calculated after selecting the part of the Mg slab structure close to the bulk. The $\Delta V$ was then added to the $E_{average}$, and the corrected Fermi level was obtained. The corrected work function is given as follows:

$$\phi_{correct} = \Phi_{vac} - \left(\Delta V + E_{average}\right) \quad [2]$$
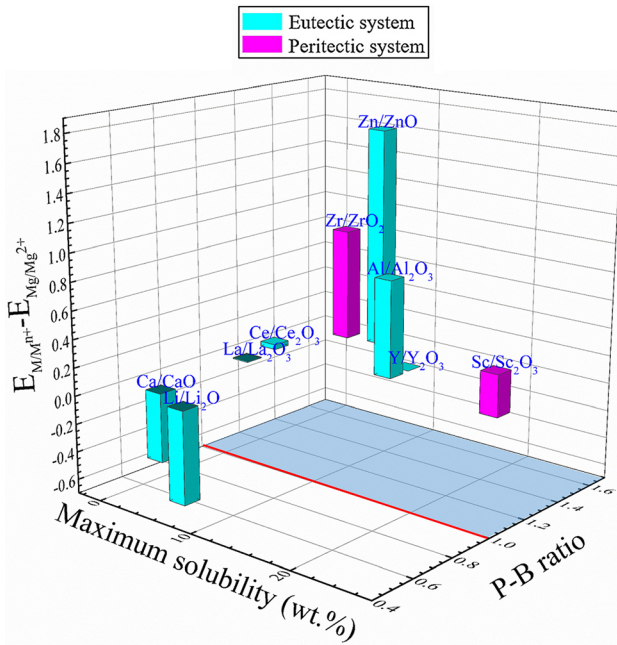


Fig. 1—Maximum solubility of alloying elements in Mg (in terms of P–B ratio and relative electrode potential *vs* Mg/Mg$^{2+}$).
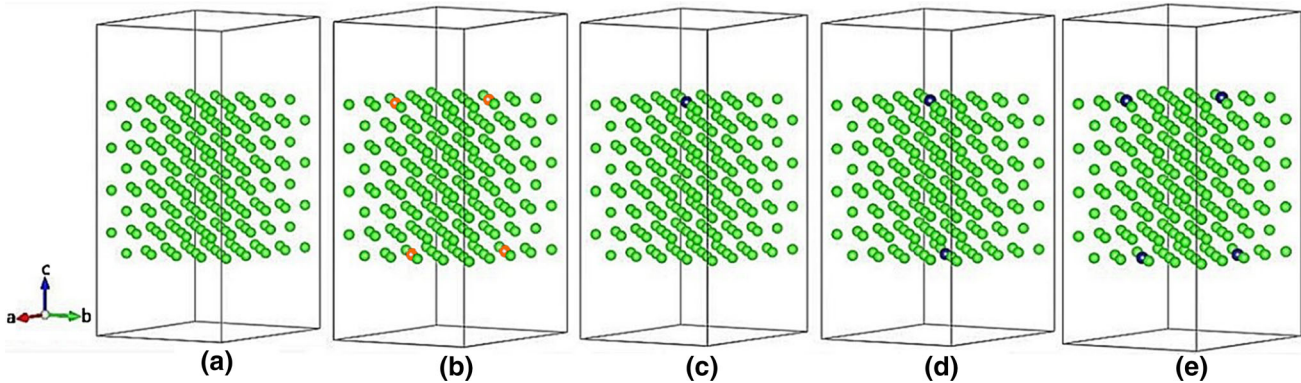


Fig. 2—Calculation slab model of (*a*) pure Mg (0001), Mg (0001) slab with (*b*) 4 Sc atoms replaced (Mg-3.6 wt pct Sc), (*c*) 1 Y atom replaced (Mg-1.8 wt pct Y), (*d*) 2 Y atoms replaced (Mg-3.5 wt pct Y), and (*e*) 4 Y atoms replaced (Mg-6.9 wt pct Y). Atoms are colored by type: Mg (green), Sc (yellow), and Y (blue) (Color figure online).

The work function values of pure Mg (0001) and Mg-Sc as well as Mg-Y solid solutions, as determined *via* DFT calculations, are shown in Table I and Figure 3. As the results show, when Mg atoms are replaced by Sc and Y in the pure slab, the work function decreases. Moreover, the work function would decrease further with the increase of Y addition, consistent with the results of a previous study.[24] However, the value of the work function difference ($\delta$) between Mg-3.6Sc and Mg-1.8Y is considerably smaller than that between Mg-3.6Sc and pure Mg. This suggests that small addition of Y atoms to Mg will lower the driving force of micro-galvanic corrosion caused by segregation. Therefore, ternary Mg-Sc-Y alloys with different concentrations of Y were

produced to verify the improvement in the corrosion resistance.

## III. EXPERIMENTS PROCEDURE

### A. *Test Material*

Based on calculation results, ternary Mg-4 wt pct Sc-*x* wt pct Y ($x$ = 0, 0.5, 1, 2, 2.5, 3.5) alloys were designed. The alloys were fabricated by melting the corresponding amounts of the pure Mg (99.99 pct), Mg-30 wt pct Sc, and Mg-15 wt pct Y intermediate alloys (melting and refining temperature: 730 °C). Afterward, the melt was poured into a pre-heated steel mold under the protective argon (Ar) atmosphere. The actual chemical composition of each alloy (see Table II) was determined by means of inductively coupled plasma spectroscopy (ICP-AES, Thermo iCAP7600). A good correspondence between the nominal and the actual alloy concentrations was realized.

### B. *Specimen Preparation and Characterization*

The microstructure was observed *via* optical microscopy (OM, Zeiss Axio Observer A1), as well as field-emission scanning electron microscopy (SEM, FEI Sirion 200) combined with energy dispersive X-ray spectroscopy (EDS). The OM and SEM specimens were progressively ground on SiC abrasive paper (320, 2000, 3000, 7000 grit), and then polished with an $Al_2O_3$ aqueous solution. The polished specimens for OM observation were chemically etched in a 4 pct nitric acid alcohol solution to reveal the grain boundaries. The phases constituent were identified by X-ray diffraction (XRD, Bruker D8 ADVANCE Da Vinci) with 3kW Cu-K$\alpha$ radiation.

The relative Volta potential fluctuation of different structures was measured by means of scanning Kelvin probe force microscopy (SKPFM, Bruker Dimension Icon & FastScan Bio), which revealed the surface morphology and potential difference trends of the specimens. The distance between the scanning probe and the specimen was 80 $\mu$m. In preparation for the measurements, each specimen was mechanically ground and polished, etched with a 4 pct nitric acid alcohol solution, rinsed with alcohol, and dried in warm flowing air.

**Table I.  Work Function of Slab Models, $\delta$ is the Work Function Difference Value Between Mg-3.6Sc and Other Slabs**

| Dopant (Weight Percent) | Work Function (eV) | $\delta$ (eV) |
| --- | --- | --- |
| Pure | 3.766 | 0.021 |
| Mg-3.6Sc | 3.745 | — |
| Mg-1.8Y | 3.740 | 0.005 |
| Mg-3.5Y | 3.719 | 0.026 |
| Mg-6.9Y | 3.664 | 0.081 |



Fig. 3—Calculated work function of pure Mg, Mg-(Sc), and Mg-(Y) slab models.

**Table II.  Actual Compositions (Weight Percent) of the Mg-Sc-Y Alloys**

| Alloys | Sc | Y | Fe | Cu | Ni | Mg |
| --- | --- | --- | --- | --- | --- | --- |
| Mg-4Sc | 4.2860 | — | 0.0140 | 0.0022 | 0.0017 | bal. |
| Mg-4Sc-0.5Y | 4.2220 | 0.5535 | 0.0105 | 0.0065 | 0.0018 | bal. |
| Mg-4Sc-1Y | 4.2030 | 1.2680 | 0.0106 | 0.0123 | 0.0021 | bal. |
| Mg-4Sc-2Y | 4.0960 | 1.9010 | 0.0140 | 0.0193 | 0.0024 | bal. |
| Mg-4Sc-2.5Y | 4.0020 | 2.7040 | 0.0171 | 0.0261 | 0.0020 | bal. |
| Mg-4Sc-3.5Y | 3.9880 | 3.4830 | 0.0195 | 0.0354 | 0.0015 | bal. |

The corrosion products were analyzed *via* electrolyte X-ray photoelectron spectroscopy (XPS, Kratos AXIS UltraDLD) using a monochromatic Al-Kα ray. Prior to the XPS measurements, the specimens were immersed in a 3.5 wt pct NaCl solution for 3600 seconds.

## C. *Corrosion Tests*

The corrosion tests performed in this work included mainly hydrogen ($H_2$) collection, immersion, and electrochemical measurements. The specimens for corrosion tests were all ground with 3000 grit SiC abrasive paper, and rinsed with water as well as ethanol prior to the tests. The $H_2$ collection and immersion measurement were conducted in 3.5 wt pct NaCl solution at room temperature in neutral pH value without aeration. Each measurement was replicated at least three times to confirm the reliability of the results.

For $H_2$ collection, the specimens were suspended with a nylon string in the NaCl solution under an inverted glass funnel, and an acid burette was used to collect the $H_2$ produced. A detailed description of the apparatus can be found elsewhere.[30] During the immersion tests, the specimens were immersed in the NaCl solution for 72 hours. The corrosion products were removed using a solution composed of a 200 g/L chromate acid solution, 10 g/L silver nitrate, and 20 g/L barium nitrate according to ASTM G1-03. The weight loss was determined by recording the weight before and after the immersion test. The error bars for hydrogen evolution and weight loss tests were corresponding to the standard deviation of at least three measurements performed on different specimens of each alloy.

Polarization curves were measured by a PARSTAT 2273 electrochemical workstation in the NaCl solution. A three-electrode cell (a saturated calomel electrode (SCE) as the reference electrode, a high-purity platinum filament as the counter electrode and the specimen as the working electrode) was employed for the tests. The specimens were embedded in epoxy resin to realize a 1.0 cm$^2$ insulation area with the electrolyte. The open circuit potential (OCP) measurements were performed immediately after the working electrode was immersed in the NaCl solution. After 3600 seconds, the OCP was relatively stable. The polarization test was conducted at a scan rate of 1 mV/s, and the potential scan started at − 300 mV *vs* corrosion potential ($E_{corr}$) to the pitting potential. Subsequently, the specimens were immediately washed with distilled water and dried in warm air, and optical photos were taken to compare the morphology of the ternary Mg-Sc-Y alloys.

## IV. RESULTS

### A. *Microstructural Characterization*

Figure 4 shows the optical micrographs of the Mg-Sc-Y alloys. The Mg-4Sc, Mg-4Sc-0.5Y, Mg-4Sc-1Y, Mg-4Sc-2Y, Mg-4Sc-2.5Y, and Mg-4Sc-3.5Y alloys are characterized by grain sizes of $118 \pm 7$, $99 \pm 7$, $92 \pm 7$, $88 \pm 6$, $85 \pm 7$, and $82 \pm 5$ $\mu$m, respectively,

measured *via* the linear intercept method.[31] The grain size decreases gradually with increasing Y content, consistent with previously reported studies.[32–34] Each ternary Mg-Sc-Y alloy is composed of the typical peritectic microstructure with cellular grains, irrespective of the Y concentration. According to the phase graphs,[18] the Mg-Sc binary alloy is a peritectic system, and the Mg-Y alloy is a eutectic system. During non-equilibrium solidification, elemental Sc segregates (in general) into the intergranular cells and pushes Y to the surrounding areas. The SEM and EDS results of the Mg-4Sc, Mg-4Sc-1Y, and Mg-4Sc-3.5Y alloys (see Figure 5) confirm the presence of segregated Sc (Sc-rich zone) and Y (Sc-depleted zone) in the Mg matrix. Furthermore, the XRD pattern of the Mg-Sc-Y alloys, shown in Figure 6, consists of α-Mg peaks only, indicating that these alloys are in the single-phase state.

### B. *Corrosion Results*

#### 1. *Immersion Tests*

Figure 7 shows the hydrogen evolution of the Mg-Sc-Y alloys immersed in the 3.5 wt pct NaCl for 24 and 72 hours. The corrosion rates of these alloys can be ranked as follows: Mg-4Sc >> Mg-4Sc-3.5Y > Mg-4Sc-2.5Y > Mg-4Sc-2Y > Mg-4Sc-0.5Y > Mg-4Sc-1Y. For each specimen, the amount of evolved $H_2$ increases monotonically with collection time, but the slope of the increase differs distinctly with the concentration of Y. The difference between the $H_2$ evolution volume of the Mg-4Sc and Mg-4Sc-*x*Y ($x$ = 0.5, 1, 2, 2.5, 3.5) alloys is initially small, but becomes extremely large with increasing immersion time. For example, the $H_2$ volume of the Mg-4Sc alloy is two times larger than that of the Mg-4Sc-1Y alloy on the first day, but is almost ten times larger after 72 hours (third day).

The variation in the weight loss is shown in Figure 8, which reveals a trend analogous to that of the hydrogen collection. The corrosion rates decrease initially in low-Y-containing alloys, and increase with the increasing of Y content thereafter. However, the corrosion rate of Mg-4Sc-3.5Y (the highest Y-containing alloy) is substantially lower than that of the binary Mg-Sc alloy. Thus, Y addition yields improved corrosion resistance of the Mg-Sc alloy (see Table III for the corrosion rates determined from the hydrogen collection and weight loss tests).

#### 2. *Electrochemical measurements*

Figure 9 presents the OCP variations of the Mg-Sc-Y alloys. The OCP increase with time and reach relatively constant values. No sudden drop in potential is observed during the immersion process, indicating the passive film gradually formed would last at least 3600 seconds in this condition. With increasing Y content, the OCP value of the ternary alloys decreases initially and then increases to a higher level than that of the Mg-Sc alloy.

The potential dynamic polarization curves of the Mg-Sc-Y alloys are shown in Figure 10, at least three measurements were repeated to confirm the reliability of the results. The variation in the $E_{corr}$ with the Y content
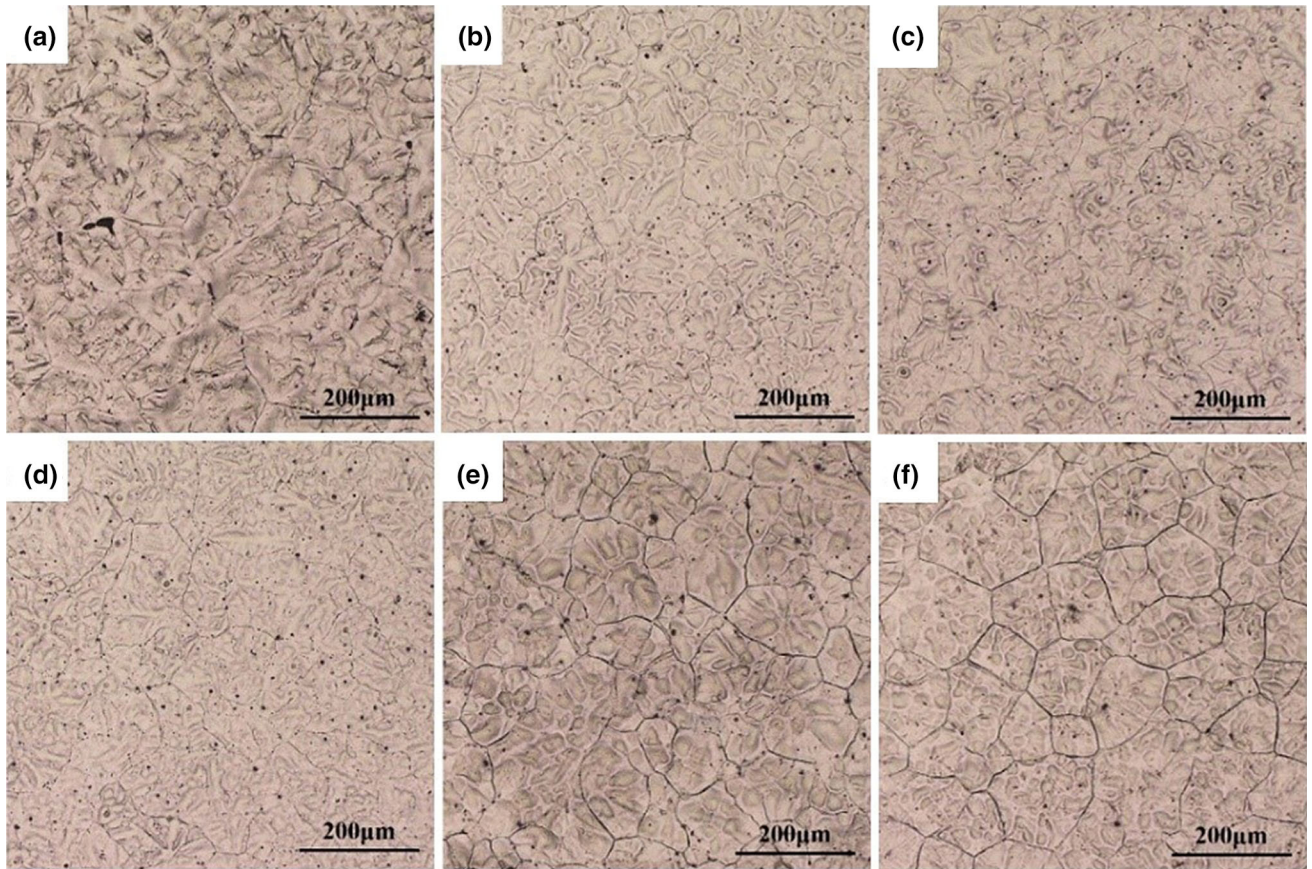
Fig. 4—Optical micrographs of (*a*) Mg-4Sc, (*b*) Mg-4Sc-0.5Y, (*c*) Mg-4Sc-1Y, (*d*) Mg-4Sc-2Y, (*e*) Mg-4Sc-2.5Y, and (*f*) Mg-4Sc-3.5Y alloys.
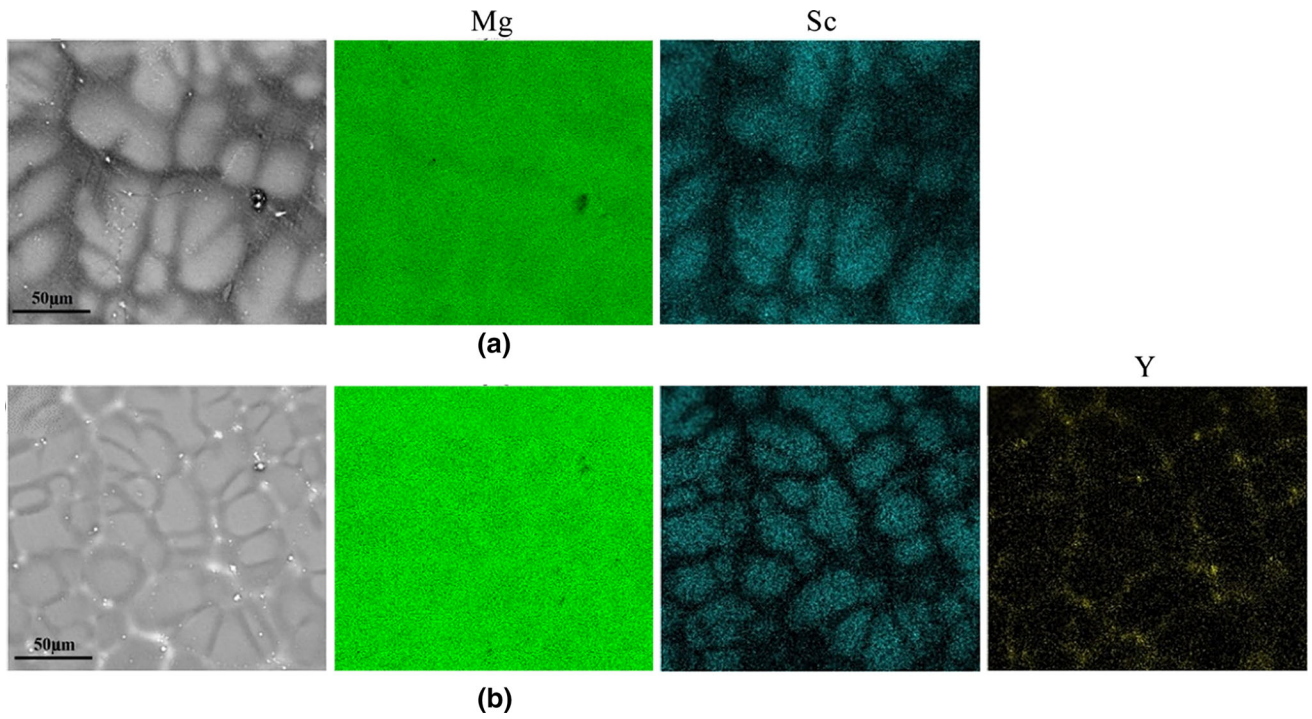


Fig. 5—SEM and EDS mapping for (*a*) Mg, Sc in Mg-4Sc and (*b*) Mg, Sc, Y in Mg-4Sc-1Y alloys.
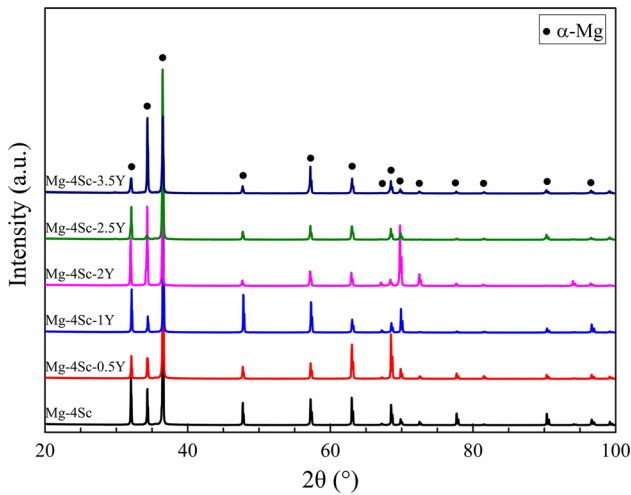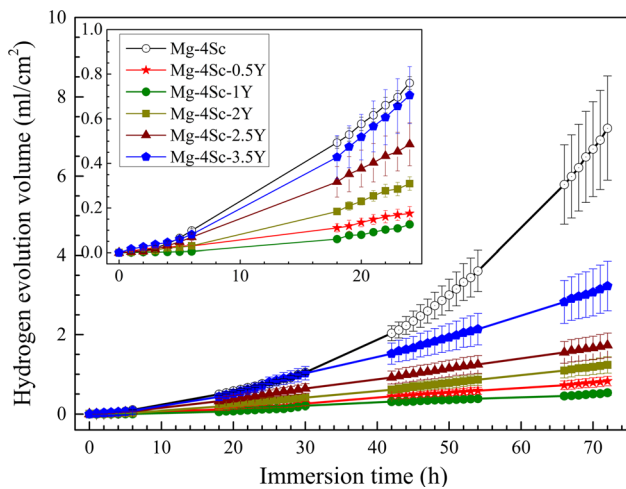
Fig. 6—XRD patterns of the Mg-Sc-Y alloys.



Fig. 7—Hydrogen evolution of the Mg-Sc-Y alloys immersed in 3.5 wt pct NaCl for 72 h, and the inset for 24 h immersion. The error bars correspond to the standard deviation based on at least three measurements performed on different specimens of each alloy.
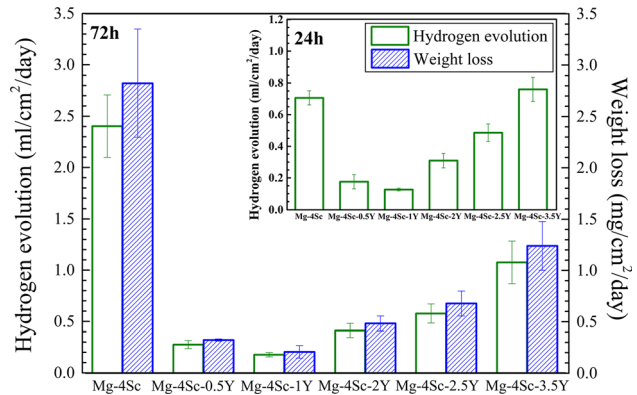


Fig. 8—Hydrogen evolution and weight loss of the Mg-Sc-Y alloys immersed in 3.5 wt pct NaCl for 72 h, and the inset for hydrogen evolution of 24 h immersion. The error bars correspond to the standard deviation based on at least three measurements performed on different specimens of each alloy.

is generally consistent with the OCP results. To elucidate the polarization behavior, the anode and cathode are separately analyzed. Regarding the anodic branch that is closely related to the dissolution of Mg,[31,35] the addition of Y could reduce the anodic current density by almost one order of magnitude (see Table IV for further details of the corrosion potential and current density). In terms of the cathodic branch that associated with the H2 evolution rate, the variation of the cathodic current density exhibits an analogous trend to that of the anodic current density. Nevertheless, the H2 evolution is accelerated slightly with the gradual increase of Y content. Moreover, the ranking of the corrosion property corresponds is in good agreement with the results of the hydrogen and weight loss measurement.

As shown in Figures 10(d) through (i), the corroded surfaces of Mg-Sc-Y alloys after the polarization tests demonstrate that these alloys undergo typical pitting corrosion. The number of detectable pitting areas is

prevalent without the addition of Y, but as the Y amount increased, the corrosion morphology shifts from mainly pitting corrosion to general corrosion. This implies that the surface layer of the Mg-Sc-Y alloys is considerably more protective than that of the Mg-Sc alloy, which is beneficial to improve the corrosion property of the alloys.

### 3. X-ray photoelectron spectroscopy (XPS)

To analyze the surface layer, XPS survey spectra were collected from the corroded specimens presented in Figure 11. The peaks of Mg, O, and Sc are observed in the spectra of the Mg-4Sc alloy. After Y addition, its characteristic peaks become discernible in the curves, which indicates the presence of Y element in the corrosion surface layer.

The structure of the corrosion product is further investigated *via* narrow scan XPS spectra presented in Figure 12. The Sc 2p peak and Y 3d peak are correspond to $Sc_2O_3$ and $Y_2O_3$, respectively, shown in the XPS Handbook.[36] To analyze the volume fraction variation of Sc and Y in the surface layer, the Mg 2p peak is set as the reference, and the peaks of other elements are adjusted proportionally. The peak intensity ratio of $Sc_2O_3$ and $Y_2O_3$, which is proportional to the volume fraction, increases significantly with the addition of Y. The P–B ratios of $Sc_2O_3$ and $Y_2O_3$ are 1.19 and 1.39, respectively, and these values are both larger than that of MgO (0.81). The presence of $Sc_2O_3$ and $Y_2O_3$ are believed to improve the completeness and protectiveness of the surface layer comprising the Mg alloys. Furthermore, the protectiveness of the surface layer seems to increase with the increasing of $Y_2O_3$ content, consistent with the variation in the pitting potential.

## V. DISCUSSION

From a thermodynamic viewpoint, the driving force of micro-galvanic corrosion in a single-phase material is attributed to the electrode potential difference between the alloying element-segregated area and the depleted

**Table III. Hydrogen Evolution (for 24 and 72 h) and Weight Loss (for 72 h) Rates of Mg-Sc-Y Alloys Immersed in 3.5 Wt Pct NaCl Solution**

| Alloys | 24 h Hydrogen Evolution (mL/cm$^2$/day) | 72 h Hydrogen Evolution (mL/cm$^2$/day) | Weight Loss (mg/cm$^2$/day) |
|---|---|---|---|
| Mg-4Sc | 0.71 | 2.40 | 2.83 |
| Mg-4Sc-0.5Y | 0.18 | 0.28 | 0.32 |
| Mg-4Sc-1Y | 0.13 | 0.18 | 0.21 |
| Mg-4Sc-2Y | 0.31 | 0.41 | 0.48 |
| Mg-4Sc-2.5Y | 0.49 | 0.58 | 0.68 |
| Mg-4Sc-3.5Y | 0.76 | 1.08 | 1.24 |
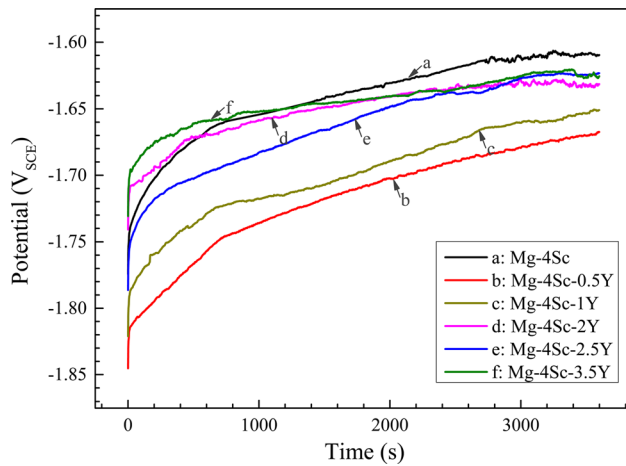


Fig. 9—Open circuit potential curves of the Mg-Sc-Y alloys immersed in 3.5 wt pct NaCl solution for 3600 s.

area. However, available corrosion data (especially the work function) on the alloying elements in the solid solution state are rather limited. In this work, DFT calculations are used to investigate the variation in the work function, *i.e.,* an indicator of the potential difference.

The work function is strongly correlated with the surface potential difference (SPD)[37] and, hence, the specimens were evaluated *via* SKPFM,[31,38] as shown in Figure 13. The potential difference value between the cellular interiors and the surrounding Mg matrix is 55 mV in the Mg-Sc alloy, and dropped to 10 mV in Mg-Sc-Y alloys. This is owing to the fact that Y segregation in Sc-depleted areas (Figure 5) helps to lower the work function difference between Sc-rich and Sc-depleted zones, leading to a substantial decrease in the driving force for micro-galvanic corrosion.

In addition to the thermodynamic factors, the corrosion kinetics plays an essential role in determining the corrosion properties. From the electrochemical results shown in Figures 9 and 10, the addition of Y can yield an increase in the pitting potential and suppress the anodic reaction. This attributes to the more protective surface layer of the Mg-Sc-Y alloys compared with that of the Mg-Sc alloy. As shown in Figure 12, the Y$_2$O$_3$ content of the surface layer increases with the increasing of Y concentration of the Mg-Sc-Y alloys. Previous

studies have reported that the oxide surface layer of pure Mg is porous and soluble in aqueous environments. Y$_2$O$_3$, in contrast, is characterized by a compact (dense) structure[39] and is stable in aqueous atmospheres. Thus, the protection provided by the surface layer is substantially enhanced, leading to a higher pitting potential and weaker Mg dissolution process than that occurring in the Mg-Sc alloy.

Regarding the cathodic branch, the process of H$_2$ evolution is slightly accelerated when Y is added to the Mg-Sc-Y alloys, owing possibly to an increase in the galvanic couple number (GCN). GCN represents the interface density between the cathode and anode. To analyze quantitatively, $P_{GCN}$ defines as the numbers of intersection points between the anode/cathode interface and the grid lines in the unit areas, which can be measured through a grid method presented in Figure 14. A detailed description of the method can be found elsewhere.[40] The $P_{GCN}$ variation is shown in Figure 15. $P_{GCN}$ increases significantly with the increasing of Y content, suggesting that the area of regions favorable for the H$_2$ evolution process increases with the Y content. Therefore, the cathodic current density of the alloys with the highest Y content (*i.e.,* Mg-4Sc-3.5Y) is dramatically larger than those of the Mg-Sc-Y alloys with low-Y content.

To elucidate the process of corrosion initiation and progression, three representative alloys Mg-4Sc, Mg-4Sc-2Y, and Mg-4Sc-5Y were immersed in a 3.5 wt pct NaCl solution for 5 minutes and 1 hour. Specimens of these alloys were examined *via* SEM and EDS (see Figure 16 for the corresponding results). After 5 minutes of immersion, similar distributions are obtained for elemental O and Y, indicating that the corrosion of the binary Mg-Sc or ternary Mg-Sc-Y alloys occurs preferentially in the Sc-depleted zones. When the immersion time is increased to 1 hour, the corrosion process is still constrained to the Sc-depleted zone, and the Sc-rich zone remains unattacked.

Figure 17 shows the corrosion morphology with corrosion product removed of Mg-4Sc, Mg-4Sc-1Y, and Mg-4Sc-3.5Y alloys immersed in 3.5 wt pct NaCl solution after 24 and 72 hours. Among these alloys, the Mg-4Sc-1Y alloy exhibits the best corrosion resistance. In particular, the surface is nearly uncorroded, except for tiny pitting areas that are observed after 24 hours of immersion. The corroded area increases noticeably
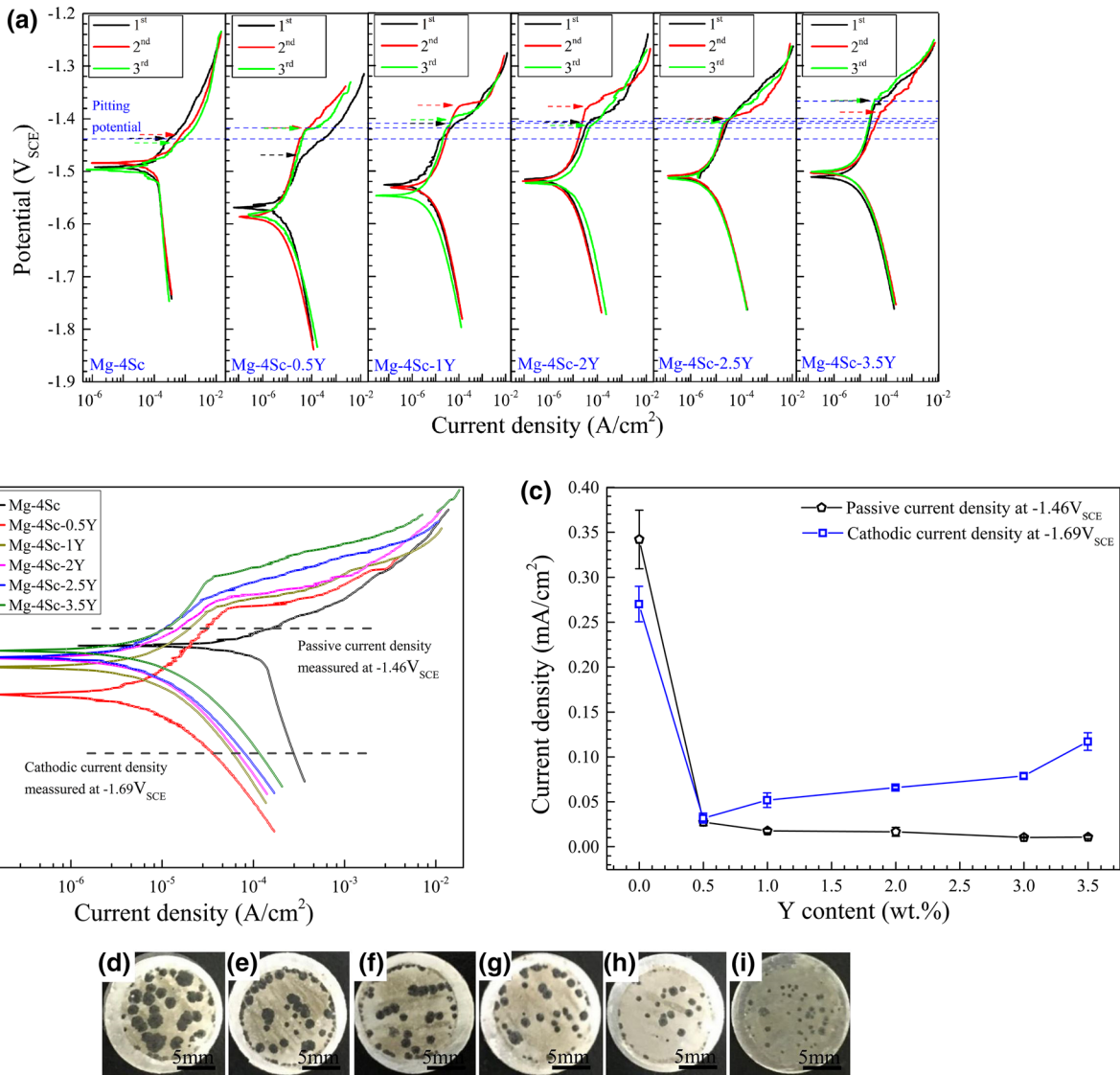
Fig. 10—(a) Polarization curves of the Mg-Sc-Y alloys measured in 3.5 wt pct NaCl solution; (b) representative polarization curves of the alloys; (c) anodic current density at − 1.46 $V_{SCE}$ and cathodic current density at − 1.69 $V_{SCE}$ of the alloys with different Y content. Corroded surfaces of the (d) Mg-4Sc, (e) Mg-4Sc-0.5Y, (f) Mg-4Sc-1Y, (g) Mg-4Sc-2Y, (h) Mg-4Sc-2.5Y, and (i) Mg-4Sc-3.5Y alloys after the polarization tests.

**Table IV. $E_{corr}$ and $I_{corr}$ of the Mg-Sc-Y Alloys Calculated from the Potential Dynamic Polarization Curves**

| Alloys | $E_{corr}$ (V) | $I_{corr}$ (mA/cm$^2$) |
|---|---|---|
| Mg-4Sc | − 1.491 | 0.153 |
| Mg-4Sc-0.5Y | − 1.579 | 0.014 |
| Mg-4Sc-1Y | − 1.534 | 0.013 |
| Mg-4Sc-2Y | − 1.518 | 0.015 |
| Mg-4Sc-2.5Y | − 1.508 | 0.018 |

when the immersion time approached to 72 hours, but intact areas (*i.e.,* the previously mentioned Sc-rich zones) are retained even in severely corroded regions. Although the micro-galvanic corrosion resistance deteriorates at high-Y content, the corrosion resistance of the Mg-4Sc-3.5Y alloy is still considerably better than that of the Mg-4Sc alloy. Cross-sectional observations reveal that the corrosion depth of the Mg-4Sc alloy is substantially larger than that of the Y-containing alloys, which is consistent with the results of the $H_2$ collection and weight loss test.

Overall, the specific peritectic microstructure determines the corrosion behavior of Mg-Sc-Y alloys, as the detailed corrosion mechanism illustration is shown in Figure 18. By adding Y into Mg-Sc alloys, the corrosion driving force decreases and more protected surface layer forms; however, the galvanic couple number tends to increase. By controlling the thermodynamics and kinetics of corrosion, Mg alloys with high corrosion resistance are designed.
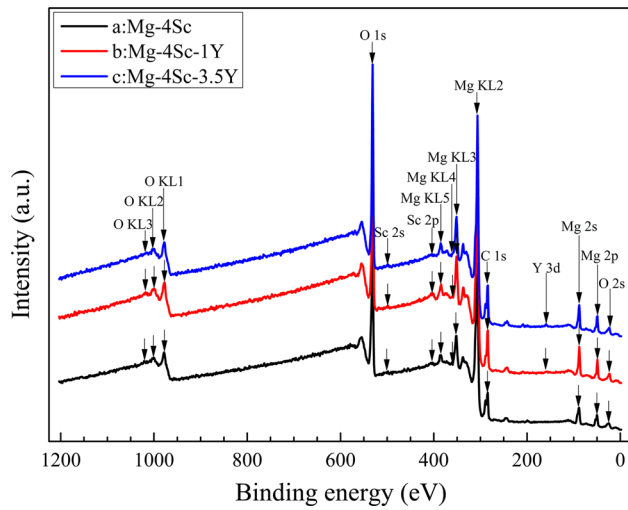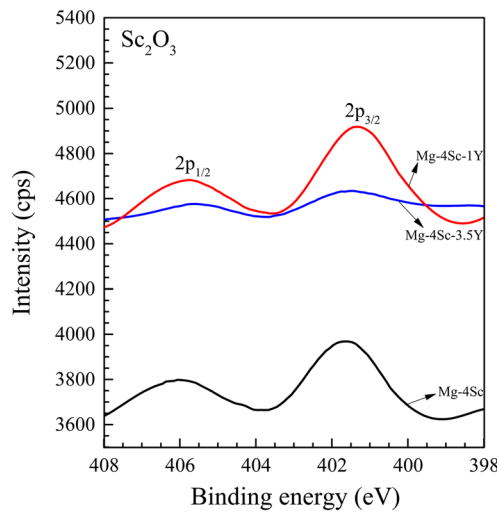
Fig. 11—XPS survey spectra of the Mg-Sc-Y alloys after immersion in 3.5 wt pct NaCl solution for 3600 s.

## VI. CONCLUSION

The Mg-4 wt pct Sc-*x* wt pct Y ($x$ = 0, 0.5, 1, 2, 2.5, 3.5) alloys are designed with the assistance of DFT calculations. The microstructure and corrosion performance of these alloys are investigated and compared. The main conclusions of this study are summarized as follows:

(1) The solid solution consists mainly of Sc and Y (without detectable levels of second phases). The Mg-Sc-Y alloys are composed of a typical peritectic microstructure with internal Sc-rich zones surrounded by Sc-depleted zones. The initiation and progression of corrosion occur mainly in the Sc-depleted zones, whereas the Sc-rich zones remain nearly intact even in severely corroded areas.

(2) The differences among the work functions of the Mg-Sc solid solution, pure Mg, and the Mg-Y solid solution are calculated by means of
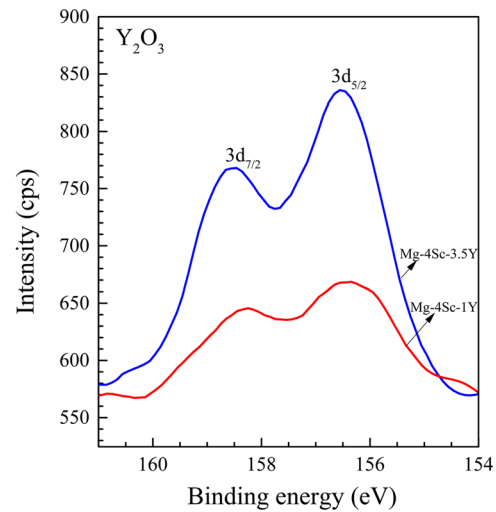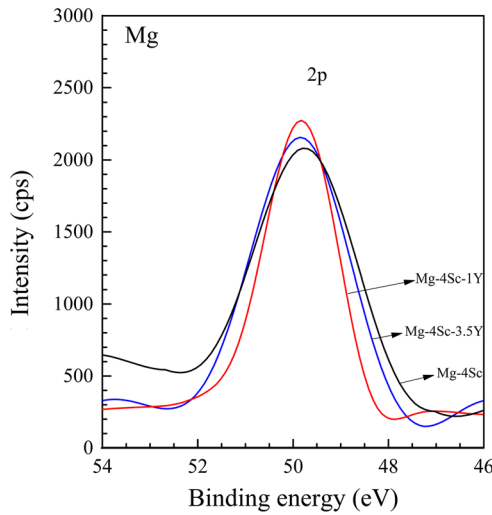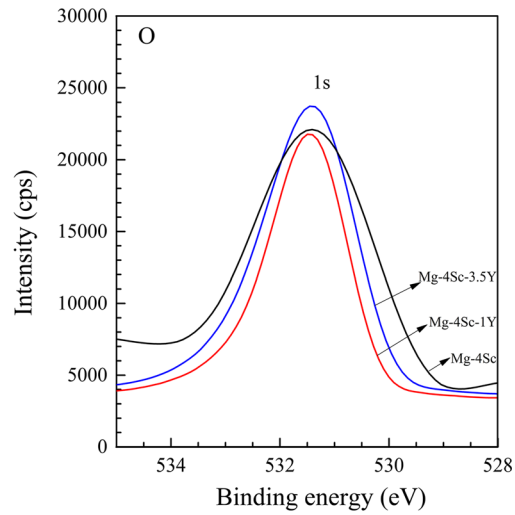


Fig. 12—Narrow scan XPS spectra of (*a*) $Sc_2O_3$; (*b*) $Y_2O_3$; (*c*) Mg; (*d*) O showing the main compositions of the passive film formed on the Mg-Sc-Y alloys; all the peaks were unified proportionally referring to the Mg 2p peaks.
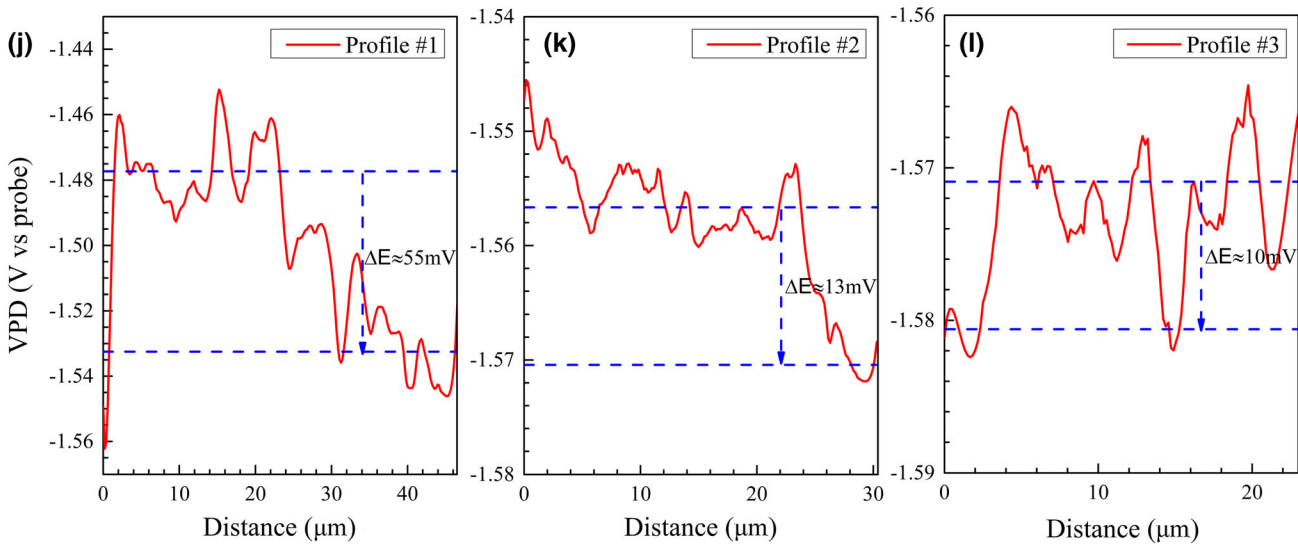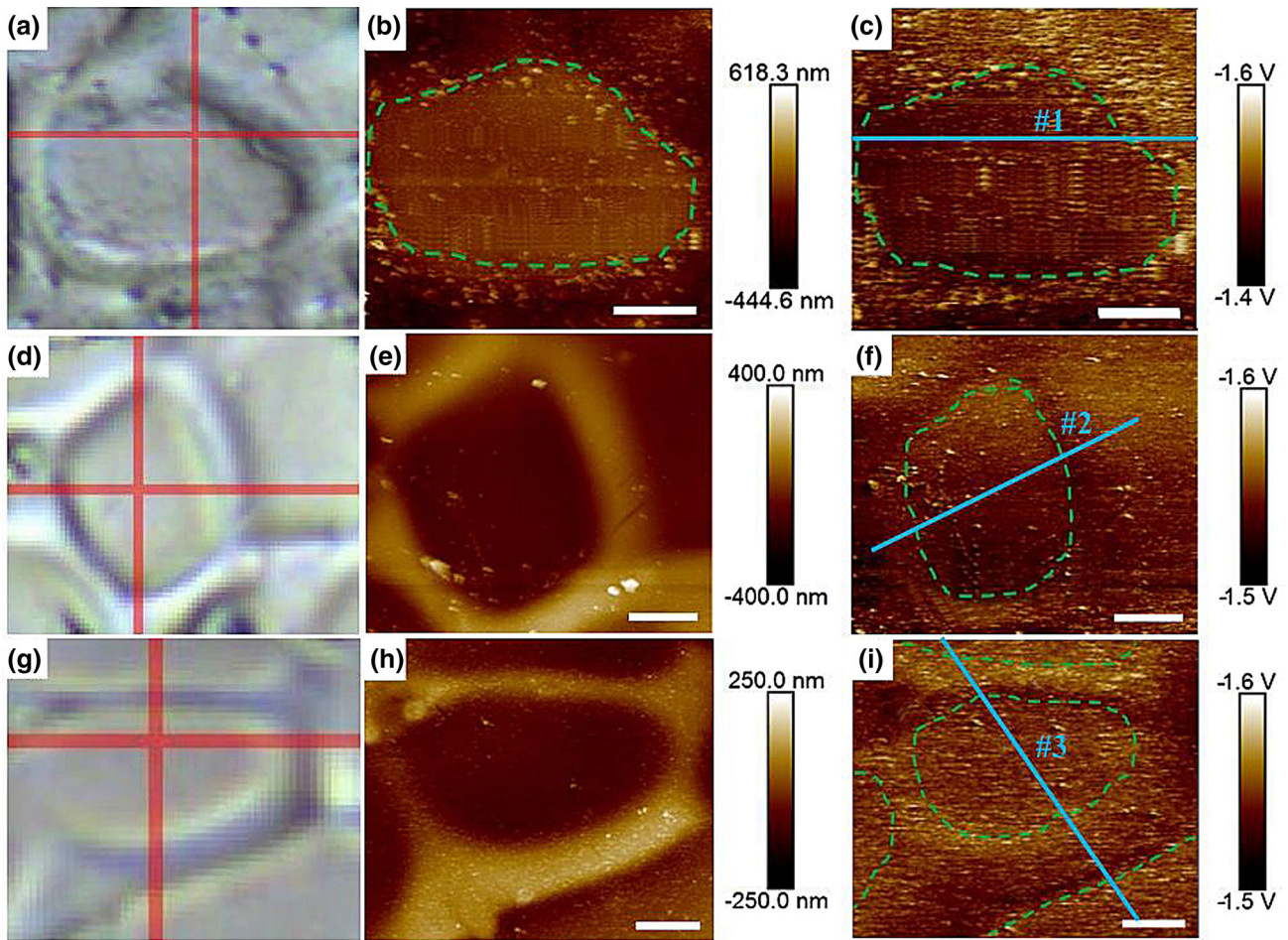
Fig. 13—SKPFM scanning photos, surface topography, potential mapping and VPD profiles associated with the blue line of (*a, b, c, j*) Mg-4Sc, (*d, e, f, k*) Mg-4Sc-1Y, and (*g, h, i, l*) Mg-4Sc-3.5Y, respectively.
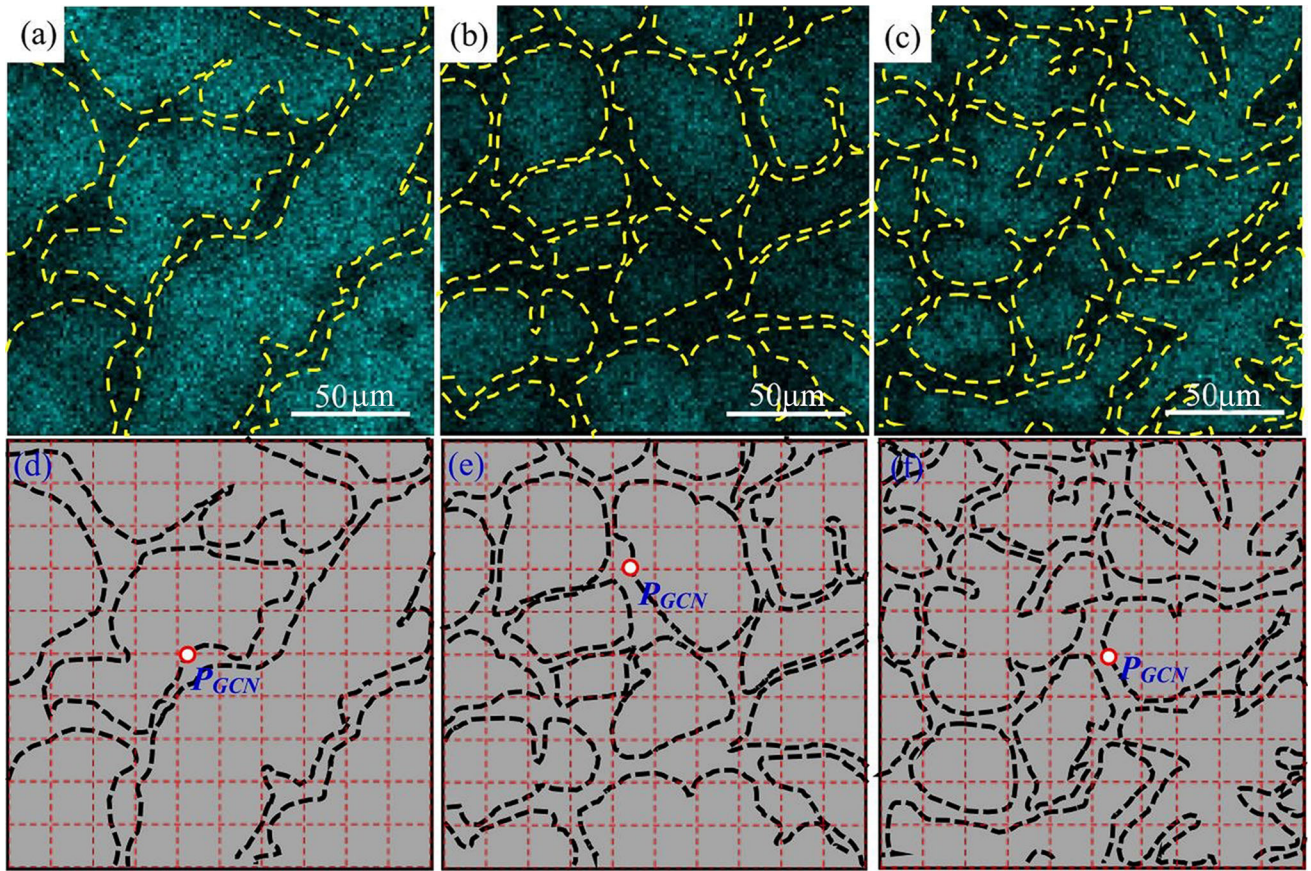
Fig. 14—Grid methods for evaluating the number of anodic and cathodic couples: SEM Sc mapping and the grid method sketch of (*a*, *d*) Mg-4Sc, (*b*, *e*) Mg-4Sc-1Y, and (*c*, *f*) Mg-4Sc-3.5Y, respectively.
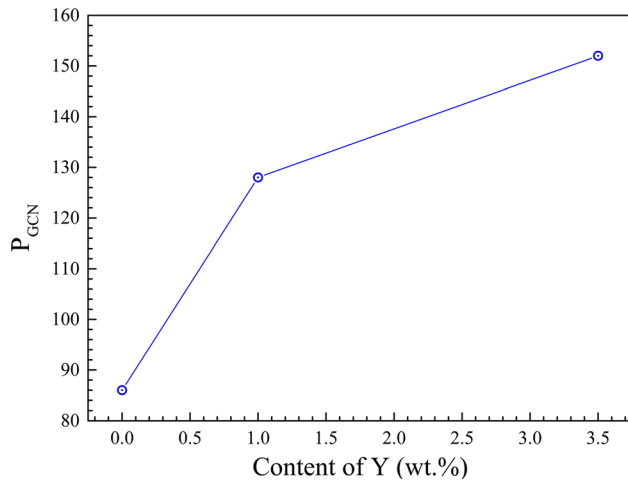


Fig. 15—Variation of $P_{GCN}$ with the Y content of the Mg-Sc-Y alloys.

first-principle calculations. The calculated differences decrease with the addition of Y, consistent with the reduction in the surface potential difference measured by SKPFM, and indicative of a decrease in the driving force for corrosion.

(3) The pitting susceptibility of the Mg alloys decreases as the amount of Y in the alloys increases. The corrosion rate of Mg-4Sc decreases significantly when Y is added to the alloy. Plotting the corrosion rate against the Y content yields a V-shaped curve. The rates can be ranked as follows: Mg-4Sc >> Mg-4Sc-3.5Y > Mg-4Sc-2.5Y > Mg-4Sc-2Y > Mg-4Sc-0.5Y > Mg-4Sc-1Y. This results mainly from two competing mechanisms, namely an improved surface layer containing $Y_2O_3$ and an increased number of micro-galvanic couples, corresponding to the anodic and cathodic kinetics, respectively.
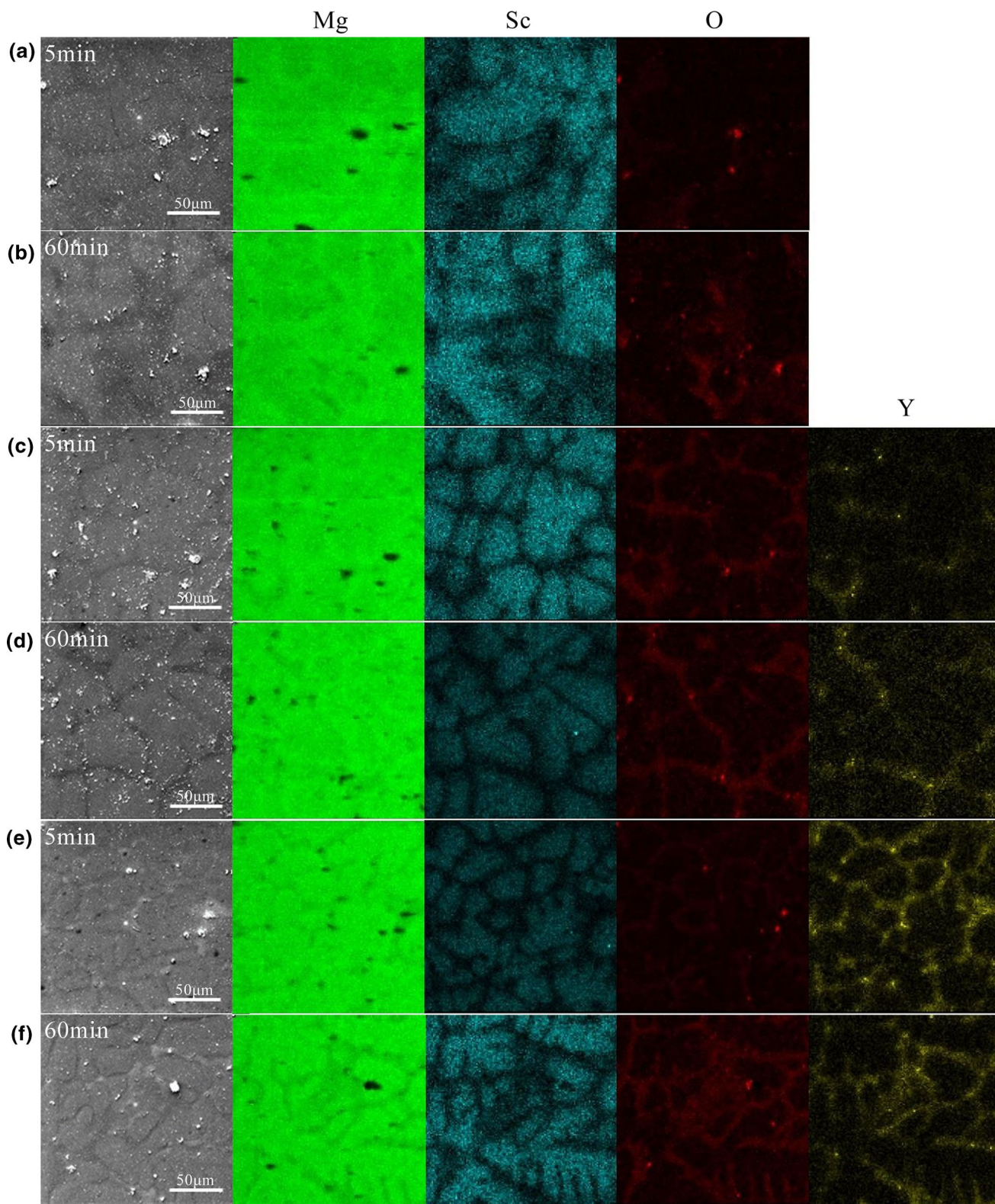
Fig. 16—SEM and EDS mapping photos for element Mg, Sc, O, Y of (*a*, *b*) Mg-4Sc, (*c*, *d*) Mg-4Sc-1Y, and (*e*, *f*) Mg-4Sc-3.5Y immersed in 3.5 wt pct NaCl solution for 5 and 60 min, respectively.
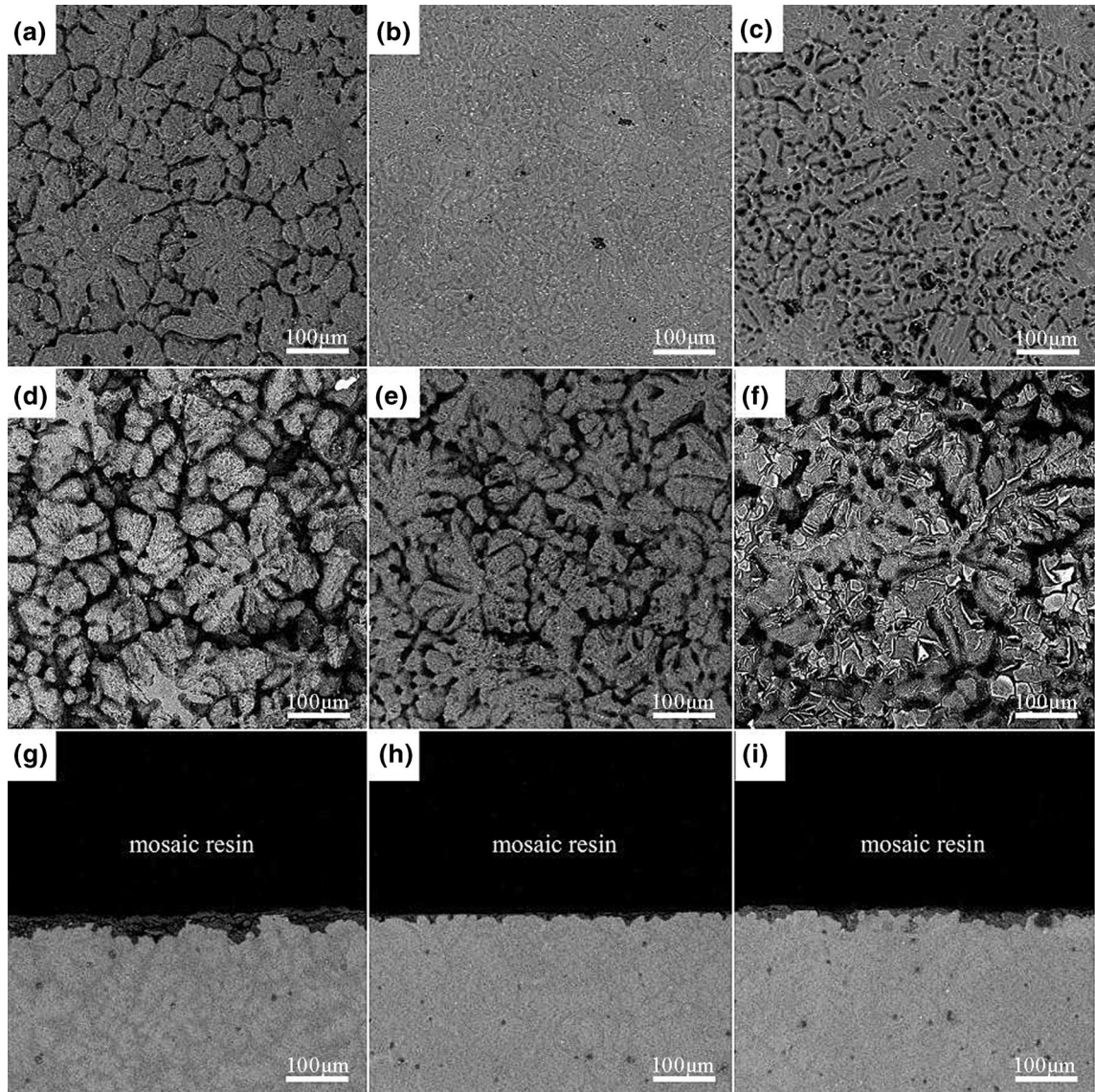
Fig. 17—Corrosion morphology of (*a, d, g*) Mg-4Sc, (*b, e, h*) Mg-4Sc-1Y, and (*c, f, i*) Mg-4Sc-3.5Y after immersion in 3.5 wt pct NaCl solution for 24, 72 h with corrosion product removed, and cross-section after immersion for 72 h, respectively.
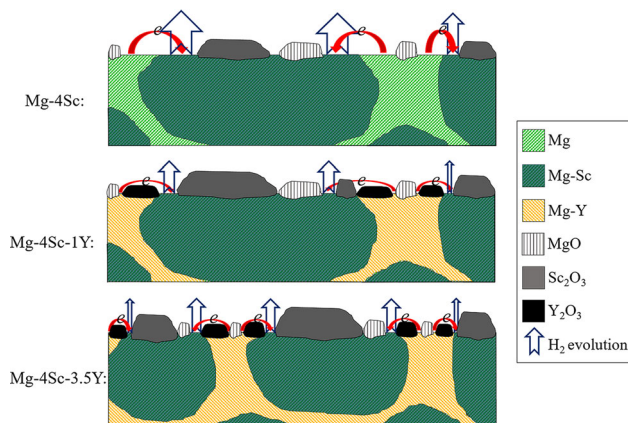


Fig. 18—Schematic diagram of the corrosion mechanism of Mg-Sc-(Y) alloys.

In conclusion, the keys of designing high corrosion resistant Mg alloys are lowering the potential difference between the cathodes and anodes, reducing the micro-galvanic couples and increasing the surface completeness. The DFT calculations may shed light on developing the novel high corrosion resistant Mg alloy system.

# REFERENCES

1. Z. Wu, R. Ahmad, B. Yin, S. Sandlöbes, and W.A. Curtin: *Science*, 2018, vol. 359, pp. 447–52.
2. A.R. Wu and C.Q. Xia: *Mater. Des.*, 2007, vol. 28, pp. 1963–67.
3. C.H. Caceres: *Metall. Mater. Trans. A Phys. Metall. Mater. Sci.*, 2007, vol. 38A, pp. 1649–62.
4. S. Eslami, M. Hasbullah, and H. Jafari: *Mater. Des.*, 2011, vol. 32, pp. 2596–2603.
5. W. Xu, N. Birbilis, G. Sha, Y. Wang, J.E. Daniels, Y. Xiao, and M. Ferry: *Nat. Mater.*, 2015, vol. 14, pp. 1229–35.
6. M. Esmaily, J.E. Svensson, S. Fajardo, N. Birbilis, G.S. Frankel, S. Virtanen, R. Arrabal, S. Thomas, and L.G. Johansson: *Prog. Mater. Sci.*, 2017, vol. 89, pp. 92–193.
7. A. Atrens, G.L. Song, M. Liu, Z. Shi, F. Cao, and M.S. Dargusch: *Adv. Eng. Mater.*, 2015, vol. 17, pp. 400–53.
8. S. Virtanen: *Mater. Sci. Eng. B Solid-State Mater. Adv. Technol.*, 2011, vol. 176, pp. 1600–08.
9. G. Song and A. Atrens: *Adv. Eng. Mater.*, 2007, vol. 9, pp. 177–83.
10. R. Xin, B. Li, L. Li, and Q. Liu: *Mater. Des.*, 2011, vol. 32, pp. 4548–52.
11. S. Thomas, N.V. Medhekar, G.S. Frankel, and N. Birbilis: *Curr. Opin. Solid State Mater. Sci.*, 2015, vol. 19, pp. 85–94.
12. K. Gusieva, C.H.J. Davies, J.R. Scully, and N. Birbilis: *Int. Mater. Rev.*, 2015, vol. 60, pp. 169–94.
13. G.L. Song and D.H. Stjohn: *Index-Corrosion of Magnesium Alloys*, Woodhead, Cambridge, 2011, pp. 618–40.
14. G. Song, B. Johannesson, S. Hapugoda, and D. StJohn: *Corros. Sci.*, 2004, vol. 46, pp. 955–77.
15. Y. Ding, C. Wen, P. Hodgson, and Y. Li: *J. Mater. Chem. B*, 2014, vol. 2, pp. 1912–33.
16. M.M. Avedesian and H. Baker: *ASM Specialty Handbook—Magnesium and Magnesium Alloys*, ASM International, Materials Park, 1999, pp. 194–210.
17. M. Pourbaix: *Atlas of Electrochemical Equilibria in Aqueous Solutions*, 2nd ed., NACE International, Houston, 1974, pp. 122–428.
18. C.M. Liu, X.R. Zhu, and H.T. Zhou: *Magnesium Alloy Phase Atlas*, Central South University Press, Changsha, 2006, pp. 4–320.
19. C. Xu and W. Gao: *Mater. Res. Innov.*, 2000, vol. 3, pp. 231–35.
20. H.S. Brar, J.P. Ball, I.S. Berglund, J.B. Allen, and M.V. Manuel: *Acta Biomater.*, 2013, vol. 9, pp. 5331–40.
21. Y.C. Lee, A.K. Dahle, and D.H. Stjohn: *Metall. Mater. Trans. A Phys. Metall. Mater. Sci.*, 2000, vol. 31, pp. 2895–2906.
22. J. Meng, W. Sun, Z. Tian, X. Qiu, and D. Zhang: *Corrosion Performance of Magnesium (Mg) Alloys Containing Rare-Earth (RE) Elements*, Woodhead, Cambridge, 2013, pp. 38–58.
23. N.D. Lang and W. Kohn: *Phys. Rev. B*, 1971, vol. 3, pp. 1215–23.
24. Z. Luo, H. Zhu, T. Ying, D. Li, and X. Zeng: *Surf. Sci.*, 2018, vols. 672–673, pp. 68–74.
25. G. Kresse and J. Hafner: *Phys. Rev. B*, 1993, vol. 47, pp. 558–61.
26. J.P. Perdew, K. Burke, and M. Ernzerhof: *Phys. Rev. Lett.*, 1996, vol. 77, pp. 3865–68.
27. P.E. Blöchl: *Phys. Rev. B*, 1994, vol. 50, pp. 17953–79.
28. N.E. Singh-Miller and N. Marzari: *Phys. Rev. B Condens. Matter Mater. Phys.*, 2009, vol. 80, pp. 1–9.
29. R. Ramprasad, P. Allmen, and L.R.C. Fonseca: *Phys. Rev. B Condens. Matter Mater. Phys.*, 1999, vol. 60, pp. 6023–27.
30. G. Song, A. Atrens, and D. Suohn: *Essent. Read. Magn. Technol.*, 2014, vol. 9781118858, pp. 565–72.
31. H.J. Kim, B. Kim, S.M. Baek, S.D. Sohn, H.J. Shin, H.Y. Jeong, C.D. Yim, B.S. You, H.Y. Ha, and S.S. Park: *Corros. Sci.*, 2015, vol. 95, pp. 133–42.
32. Q. Zhang, Q.A. Li, J. Chen, and X.Y. Zhang: *Adv. Mater. Res.*, 2013, vols. 750–752, pp. 603–06.
33. H. Xu, X. Zhang, K. Zhang, Y. Shi, and J. Ren: *J. Rare Earths*, 2016, vol. 34, pp. 315–27.
34. Q. Peng, J. Meng, Y. Li, Y. Huang, and N. Hort: *Mater. Sci. Eng. A*, 2011, vol. 528, pp. 2106–09.
35. H.Y. Ha, J.Y. Kang, C.D. Yim, J. Yang, and B.S. You: *Corros. Sci.*, 2014, vol. 89, pp. 275–85.
36. J.F. Moulder, J. Chastain, and R.C.J. King: *Handbook of x-ray photoelectron spectroscopy: a reference book of standard spectra for identification and interpretation of XPS data*, Physical Electronics, Chanhassen, 2008, pp. 29–174.
37. S.N. Mathaudhu, A.A. Luo, N.R. Neelameggham, E.A. Nyberg, and W.H. Sillekens: *Essential Readings in Magnesium Technology*, Wiley-Tms, New Jersey, 2014, pp. 581–84.
38. M. Mohedano, C. Blawert, K.A. Yasakau, R. Arrabal, E. Matykina, B. Mingo, N. Scharnagl, M.G.S. Ferreira, and M.L. Zheludkevich: *Mater. Charact.*, 2017, vol. 128, pp. 85–99.
39. P.L. Chen and I.W. Chen: *J. Am. Ceram. Soc.*, 1996, vol. 79, pp. 1801–09.
40. M. Grimm, A. Lohmüller, R.F. Singer, and S. Virtanen: *Corros. Sci.*, 2019, vol. 155, pp. 195–208.